PASJ: Publ. Astron. Soc. Japan **60**, 1347–1362, 2008 December 25

Multi-Object Infrared Camera and Spectrograph (MOIRCS) for the Subaru Telescope* I. Imaging

Ryuji SUZUKI,[1,2] Chihiro TOKOKU,[1,2] Takashi ICHIKAWA,[2] Yuka Katsuno UCHIMOTO,[1,2,3] Masahiro KONISHI,[1,2] Tomohiro YOSHIKAWA,[1,2] Ichi TANAKA,[1,2] Toru YAMADA,[1,2] Koji OMATA,[1] and Tetsuo NISHIMURA[1]

[1]*Subaru Telescope, National Astronomical Observatory of Japan, 650 North A'ohoku Place, Hilo, HI 96720, USA*
ryuji@subaru.naoj.org

[2]*Astronomical Institute, Tohoku University, Aramaki, Aoba-ku, Sendai, 980-8578*

[3]*Institute of Astronomy, The University of Tokyo, Osawa, Mitaka, Tokyo 181-0015*

(Received 2007 July 23; accepted 2008 July 11)

Abstract

MOIRCS is a fully cryogenic near-infrared instrument for the 8.2 m Subaru Telescope. MOIRCS has two observation modes: a wide-field imaging mode and a multiobject spectroscopy mode. This paper describes the imaging mode, its specifications, and actual performances that we confirmed through laboratory tests and commissioning observations. The imaging mode provides a $4' \times 7'$ field of view with a pixel scale of $0\farcs117\,\mathrm{pixel}^{-1}$ in the wavelength range of 0.85 to $2.5\,\mu\mathrm{m}$ using cooled optics and two 2048×2048 HgCdTe HAWAII-2 focal plane arrays. Good-quality images are obtained over the entire field of view with practically no chromatic aberration. The limiting magnitudes for a point source estimated from observed background brightness and throughput are 23.7 in the J band, 23.0 in the H band, and 22.6 in the K_s band (Vega) with $S/N = 5$, $0\farcs5$ seeing, $1\farcs0$ aperture, and 1 hr exposure.

Key words: infrared: general — instrumentation: detectors

1. Introduction

Exploring the universe more deeply with higher angular resolution continues to open up new frontiers in modern observational astronomy. In order to deepen and refine our new knowledge, the quantity of observed objects needs to be increased, and the quality of data needs to be improved for more accurate and statistically sound studies. This has been true for studies of high-redshift galaxies, which is one of the key subjects of modern astronomy. The study of high-redshift galaxies has been extensively investigated by optical observations from both space and ground using the Hubble Space Telescope and ground telescopes in the 8 m class. Our knowledge about star-forming galaxies in the high-redshift universe from $z = 3$ to $z = 7$ has been greatly improved in the last decade (e.g., Madau et al. 1996; Steidel et al. 1996a, 1996b, 2003; Ouchi et al. 2004; Kashikawa et al. 2006; Iye et al. 2006).

On the other hand, more normal galaxies and early type galaxies that have less intensive star-formation activity have been investigated mostly by near-infrared observations (e.g., Daddi et al. 2000, 2004; Dickinson et al. 2003; Franx et al. 2003; Kriek et al. 2008). This is because longer wavelengths beyond the 4000 Å break in the rest frame, which traces the stellar masses of galaxies, as well as most of the spectral features used for diagnosing galaxy's property are only accessible in the near-infrared region at $1.5 < z < 3$. Near-infrared observations are also essential in searching for the cosmic frontier beyond $z = 7$, because the Lyα emission line moves into the near-infrared region (Willis & Courbin 2005; Cuby et al. 2007).

Near-infrared observations, however, have been technically limited as compared with the optical counterparts. The observations were limited to only a small field of view (FOV) due to small format focal plane arrays (FPAs) available for use. A few arc-minute wide FOV of near-infrared imagers on some of telescopes in the 8 m class, and even smaller FOV of NICMOS on the Hubble Space Telescope are somewhat limited to collect a large number of objects for statistical studies. For example, a $10'$ wide FOV with a $0\farcs1$ spatial resolution would be preferred for the typical size of a local galaxy cluster at a high redshift with sufficient spatial sampling within the typical scale length of a galaxy disk. For spectroscopic observations, multiobject spectroscopy has not yet been easily achieved in the near-infrared region, due to the technical difficulty in realizing a complex cryogenic spectrograph.

Recent advancements in the aperture diameter of telescopes, large format of FPAs, quality of images with good seeing and high-performance instrument optics, high observation efficiency supported by improved observation techniques, and faster data processing all are key factors for justifying a new instrument project. Large-format FPAs as well as large optical materials become available for wide-field coverage, and mature cryogenic technology makes reliable mechanical operation under a cryogenic environment possible. In 1999, we proposed a second-generation instrument for the Subaru Telescope. The proposed instrument was named Multi-Object Infrared Camera and Spectrograph (MOIRCS). The instrument is a fully cryogenic, near-infrared, wide-field imager and a multiobject spectrograph working in the wavelength range of 0.85 to $2.5\,\mu\mathrm{m}$. The imaging mode has a $4' \times 7'$ FOV with a pixel scale of $0\farcs117\,\mathrm{pixel}^{-1}$. The FOV is 7 times larger than that of the first-generation Subaru instrument, CISCO (Motohara et al. 2002), while the pixel scales are almost identical. Early in the year,

* Based on data collected at Subaru Telescope, which is operated by the National Astronomical Observatory of Japan.

during the first-light observations, the Subaru Telescope had demonstrated superb image quality, due to excellent telescope optics and superior site seeing as good as 0.″2 (Kaifu et al. 2000). MOIRCS is designed to take full advantage of this image quality. The multi-object spectroscopy (MOS) mode is capable of $\sim$50-object simultaneous slit spectroscopy to the $K_{\rm s}$ band, which is the first to be offered as a facility instrument on a telescope in the 8 m class. MOIRCS turns out to be a versatile instrument, and is expected to produce higher-quality data than ever, not only for studying high-redshift galaxies (e.g., Kajisawa et al. 2006; Kodama et al. 2007; Ichikawa et al. 2007; Uchimoto et al. 2008), but also for many fields of astronomy.

MOIRCS was developed by a collaboration of the Subaru Telescope and Tohoku University in Japan. The conceptual design started in 1999, and after five years of detailed design, fabrication, construction, and testing, MOIRCS had its first light in 2004 September. The imaging mode and the MOS mode became available to community use in 2005 January and 2006 September, respectively. MOIRCS attempted successfully to use the new technologies, such as a field-splitting scheme, a slit mask exchanger system, and cryostat construction, in addition to some novel design features. In addition, the MOIRCS project tested a somewhat unconventional approach in order to construct it faster at lower cost. We skipped full-scale design reviews, and proceeded with progressive design refinements for noncritical subsystems, such as the mechanical, thermal, and opto-mechanical components.

In this paper, we describe the overall design of MOIRCS in section 2, individual subsystems in section 3, and the results of a performance evaluation obtained through laboratory tests and commissioning observations in section 4. The present paper mostly deals with the imaging mode, since the MOS mode is described in Tokoku et al. (2006) and Tokoku et al. (in preparation).

Table 1. Specifications of MOIRCS.

Observing mode	Imaging mode, multiobject spectroscopy mode
Wavelength	0.85 μm–2.5 μm
Field of view	$4' \times 7'$
Pixel scale	0.″117 pixel^{-1}
Detectors	Two 2048 $\times$ 2048 HgCdTe (HAWAII-2)
Filters	J, H, $K_{\rm s}$, K, $K_{\rm cont}$, H_2, CO, [Fe II]
Grisms	$\lambda/\Delta\lambda$ = 500, 1300, 3000 (with 0.″5 slit)
Size	$2 \times 2 \times 2$ m^3
Weight	2.3 t

2. Overview

Table 1 summarizes the MOIRCS specifications. The instrument has the imaging mode and MOS mode in the wavelength range of 0.85 to 2.5 μm. Two 2048 $\times$ 2048 HgCdTe HAWAII-2 FPAs cover $4' \times 7'$ with a pixel scale of 0.″117 pixel^{-1}. Standard broad-band filters (J, H, $K_{\rm s}$, and K) and narrow-band filters ($K_{\rm cont}$, H_2, CO, and [Fe II]), whose specifications follow those of the Mauna Kea consortium filter set (Tokunaga et al. 2002), are available in the imaging mode. In the MOS mode, slitlets are created on an aluminum sheet by a laser cutting machine, and the sheet held in an aluminum frame (slit mask) is placed at the telescope focal plane. Grisms with spectral resolution ($\lambda/\Delta\lambda$) of 500, 1300, and 3000 with 0.″5 slit are available as a disperser.

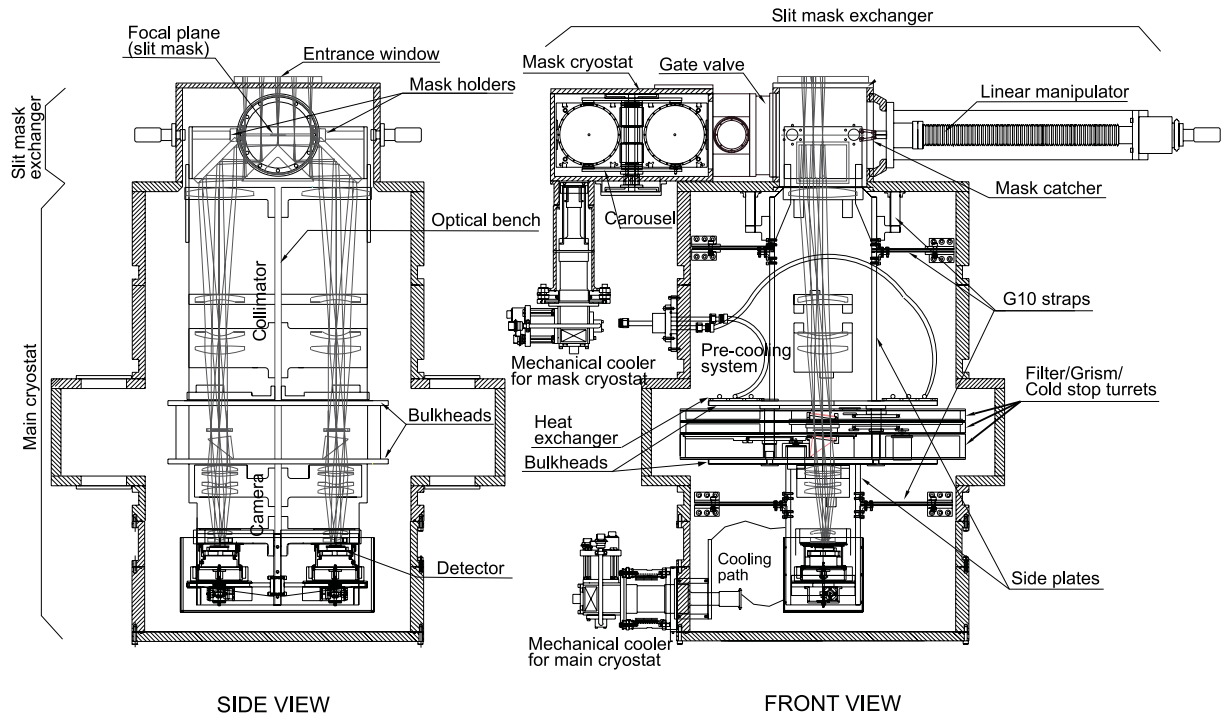

Fig. 1. Schematic drawing of MOIRCS. (Copyright SPIE [2006].)

Figure 1 shows a schematic view of the MOIRCS cryostat. The entire structure fits inside of the $2 \times 2 \times 2\,m^3$ space allowed for the standard Subaru Cassegrain instrument, and weighs 2.3 tons. Because MOIRCS is an infrared instrument reaching the K_s band, all optical components have to be housed in the cryostat, and cooled down to reduce the thermal radiation from the instrument, itself. An optical bench plate is suspended using G10 straps attached to the inside wall of the cryostat. Because the two HAWAII-2 FPAs are not abuttable, and because the optics would be prohibitively large for two FPAs abutted, the FOV is split onto two HAWAII-2 FPAs, each subtending $4' \times 3'.5$, by a roof mirror splitting the beam slightly under the telescope focal plane. Two sets of identical optics are mounted on either side of the optical bench plate. The optics consists of a collimator section and a camera section, and three turrets containing the filters and the grisms are inserted in a collimated beam between the two sections. The telescope focal plane is where the cooled slit mask is brought in from the mask cryostat by using a slit mask exchanger. The mask cryostat can be isolated from the main cryostat for changing the installed slit mask set. The mask cryostat is equipped with its own mechanical cooler to make independent cooling cycles possible. The details of this part of the cryostat are described in the MOS paper.

We determined the FOV of MOIRCS after considering that (1) the $8'$ diameter is a partially vignetted FOV of the telescope and (2) the expected best seeing size is $0''.2$–$0''.3$. We find that a $4' \times 7'$ FOV fitting into $8'$ diameter with a pixel scale of $0''.117\,pixel^{-1}$ is a reasonable choice, leaving ~ 270 pixels ($\sim 30''$) in the central area for the spectra (see figure 2).

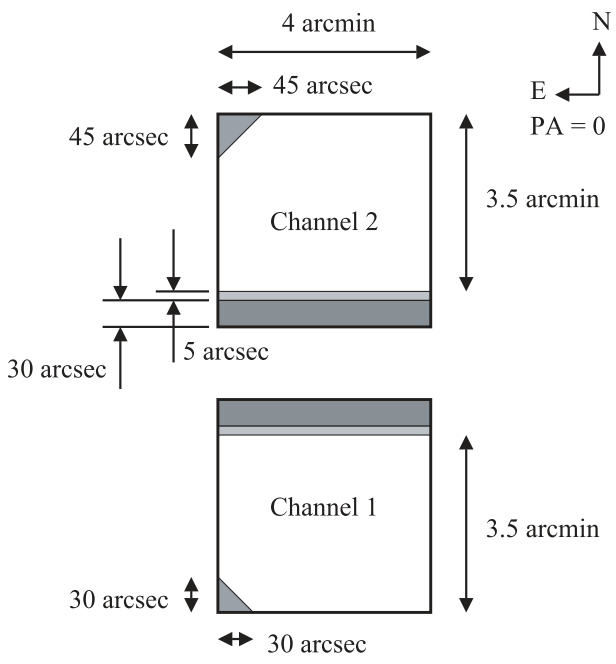

Fig. 2. Field of view of MOIRCS on the sky when the position angle is zero. Dark-gray areas at the corner of both FPAs are vignetted by the pickup mirror of adaptive optics and the telescope calibration unit. Objects in the light-gray areas are imaged on both FPAs. Dark-gray areas near the center of the field are not used in the imaging mode, but are filled with spectra in the MOS mode.

Because a ridge of the roof mirror is not located exactly on the Cassegrain focal plane, a central area of $5'' \times 4'$ along the ridge line images in both FPAs. There are two vignetting components in the MOIRCS FOV: a pickup mirror of the Adaptive Optics and a calibration unit of the telescope. Since they are at ambient temperature, the vignetted areas are darker in shorter wavelength, but brighter in longer wavelength due to thermal radiation.

3. MOIRCS Subsystems

3.1. Optics

Figure 3 shows the overall layout of the optical design. As mentioned in the previous section, the roof mirror, placed 30 mm under the telescope focal plane, feeds the telescope beam to two sets of identical optics, which reimage the telescope focal plane to the two HAWAII-2 FPAs. The roof mirror and two fold mirrors are shown on the left side of figure 3. Each set of the optics has a four-lens collimator and a six-lens camera (see table 2 for the lens parameters). The collimator not only feeds a parallel beam to the filters and the grisms, but also makes a sharp image of the telescope secondary mirror for a cold stop to be placed. The camera focuses the parallel beam onto the FPA with $0''.117\,pixel^{-1}$. The focal length and the focal ratio of the collimator are 620 mm and f/12.4, and those of the camera are 196 mm and f/3.92. The total length of the optical path is 1445 mm.

We use CaF_2, BaF_2, ZnSe, and fused silica as the lens materials, because of the availability of a large-size material, well-established refractive indices at 77 K, good transmission in the near-infrared region, and ease of fabrication and handling. The roof mirror and the fold mirrors are made of ultralow expansion glass, and are coated with gold. We use CaF_2 as a window material because its high transmission to the mid-infrared region and good heat conductivity prevent the condensation of water vapor on the window surface. The refractive indices of the lens materials at 77 K are calculated by using the temperature-dependent Sellmeier dispersion model (Tropf 1995). The parameters of the model for fused silica are derived from the refractive indices at various temperatures, which are available in Malitson (1965) and Yamamuro et al. (2006). The thermal-expansion data for the lens materials to 77 K, which have been successfully used for other near-infrared instruments, are obtained from various sources.

We designed the optics by the following steps. We adopted CaF_2-Fused Silica-ZnSe and BaF_2-Fused Silica-ZnSe apochromatic triplets as the basic lens unit to comprise the whole optics with the minimum chromatic aberration (Ren & Allington-Smith 1999; Suzuki et al. 2003). First, the collimator was designed in a reverse direction, i.e., parallel rays were traced back from a pupil stop to the collimator. The collimator was optimized to converge the parallel beam on the Cassegrain focal plane with an exit pupil at the telescope secondary mirror position. We, then, reversed the direction of the beam by tracing from the telescope to the collimator. Final optimization of the collimator was performed for the collimated beam and the image of the telescope secondary mirror at the same time. The quality of the collimated beam was evaluated with the help of an additional paraxial lens with the same back focus

Table 2. Optics parameters.

Name	Radius† (mm)	Thickness (mm)	Diameter (mm)	Material
Cassegrain focus		291.000		
Collimator 1st	434.9088 CX	30.0000	210	CaF_2
	900.0000 CX	300.0000		
Collimator 2nd	327.5578 CX	15.0000	154	ZnSe
	294.2945 CC	111.9607		
Collimator 3rd	144.5857 CC	10.0000	154	Fused silica
	228.3623 CX	21.1272		
Collimator 4th	1379.3910 CX	25.0000	154	CaF_2
	228.4374 CX	348.3000		
Camera 1st	149.4841 CX	18.0000	110	BaF_2
	621.9062 CX	6.6669		
Camera 2nd	229.9683 CC	8.0000	110	ZnSe
	279.4311 CX	25.0000		
Camera 3rd	149.4572 CC	8.0000	110	Fused silica
	305.6290 CX	1.0000		
Camera 4th	160.0915 CX	22.0000	110	BaF_2
	353.4038 CX	109.4401		
Camera 5th	99.9655 CX	10.0000	76	Fused silica
	255.5995 CC	21.8021		
Camera 6th	43.0000 CC‡	5.0000	76	BaF_2
	Infinity	10.7216		

† CC and CX represent concave and convex surfaces, respectively.
‡ Conic constant $= -1.0$.

as its focal length, while the image quality of the pupil was evaluated with the secondary mirror as an object. The camera was, then, designed to form an image on the detector plane by compensating aberrations of the collimator. In designing the collimator and the camera, we placed the apochromatic triplets where a marginal ray is the highest to reduce the axial chromatic aberration. To the triplets are given almost the same power as the total power in each section. The spherical aberration was minimized by bending the lens parameters. The second optics components were located near to the focal planes so as to adjust other aberrations, such as coma, astigmatism, and the lateral chromatic aberration.

The designed optics shows good performance. The image size is smaller than 2-by-2 pixel square over the entire wavelength range and FOV without refocusing for different wavelengths (figure 4), indicating that the axial chromatic aberration is well corrected. The best focus positions differ by only $40\,\mu\mathrm{m}$ between the J and K_s bands. The lateral chromatic aberration is $5\,\mu\mathrm{m}$, which is smaller than the pixel size ($18\,\mu\mathrm{m}$).

Tolerance analysis is important in estimating actual performance of the designed optics when the instrument is finally assembled, and in finding the sensitivity of each tolerance item to the optical performance. In order to make a realistic estimate for each tolerance item, we broke down each item, and estimated errors in detail using manufacturing information from the lens vendor, detailed mechanism and related manufacturing errors of the lens mounts, and errors associated with the alignment method. We generated one hundred optics with a random combination of values for all tolerance items by a Monte Carlo algorithm. A certain value for a tolerance item was chosen in a way that the worst number would have a higher probability than zero. The distance between the last camera lens and the detector plane was set to be variable as this component was equipped with a focus stage, as described in subsection 3.5. The optical performance of the generated optics was evaluated by a diffraction-based image analysis. We found that good optical performance, defined by 80% of energy enclosed within 2-by-2 pixel square, could be obtained with 80% probability when the manufacturing and alignment errors were within the normal tolerance. The qualities of the pupil image and the collimated beam were found not to change significantly by a similar tolerance analysis, only for the collimator. This performance estimate turned out to be conservative, because we reoptimized the optics after we measured the dimensions of the lens mounts with a precise 3D measuring tool, and after we obtained the dimensions of the finished lenses from the lens vendor.

The opto-mechanical parts, such as the lens mounts and the optical-bench plate, were made of aluminum, Al6061-T651, because of good machinability and good thermal conductivity. The Al6061-T651 has already been heat-treated, and the thermal-contraction rate is well known. We did, however, perform a further heat treatment (uphill quenching) for the lens mounts between rough machining and the final machining to release the residual stress generated by the machining and to prevent the deformation by cooling down to 77 K. The process consists of five thermal cycles of 77 K, 373 K, and room temperature. Figure 5 shows a schematic drawing of the lens

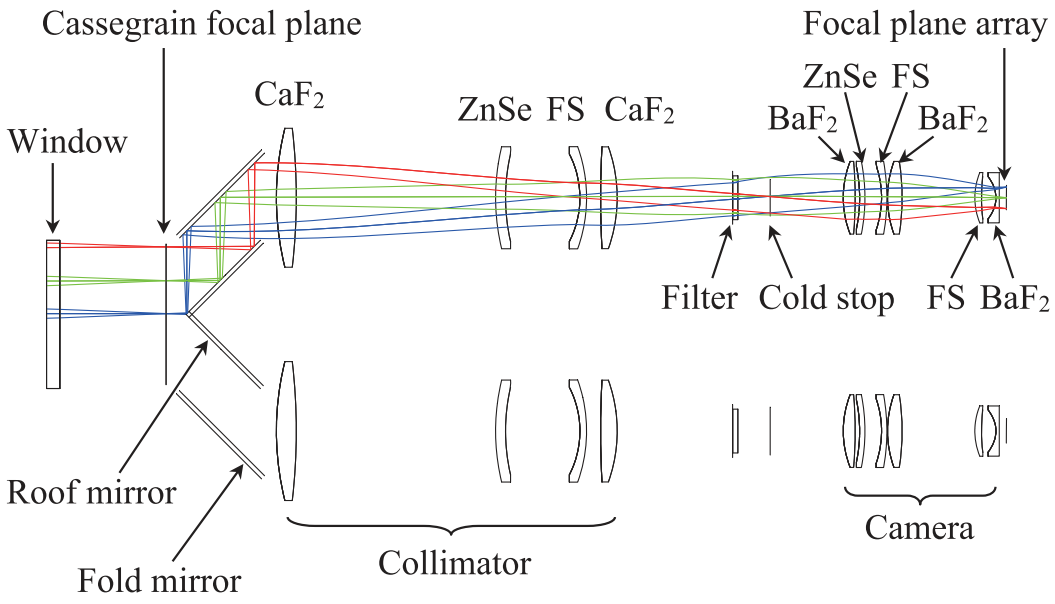

Fig. 3. Layout of the optics. (Copyright SPIE [2003].)

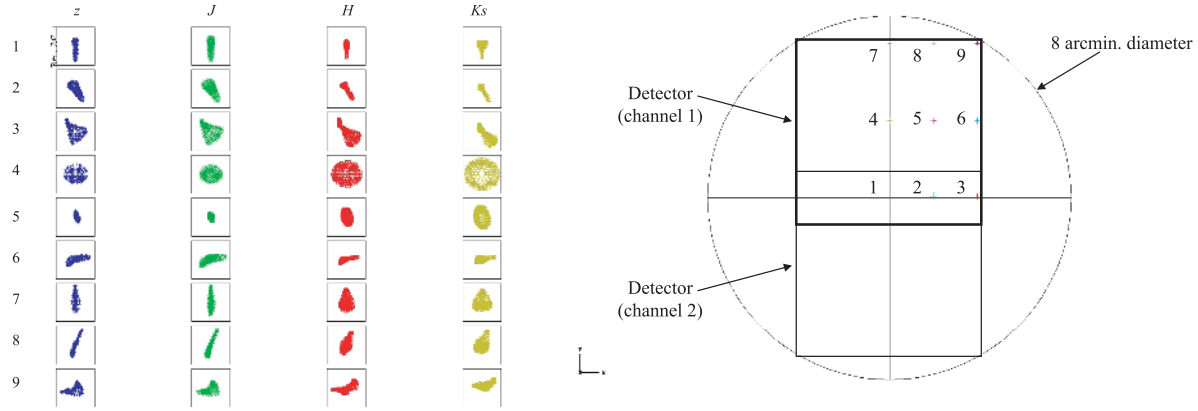

Fig. 4. Left: Spot diagrams of the imaging mode. The vertical arrangement indicates nine field positions defined in the right figure, while the horizontal arrangement indicates central wavelengths of z, J, H, and K_s bands. The box is an area of 2-pixel square. Right: Definition of the field points at the telescope focal plane. The overlapping two squares show projected coverages of the two FPAs at the telescope focal plane. (Copyright SPIE [2003].)

mount. Plate springs made of phosphor bronze hold the lens and release stress caused by a difference in thermal contraction between Al6061–T651 and the lens material. Three plate springs (spring A) retain the lens in a direction parallel to the optical axis while the other plate spring (spring B) holds the lens in a direction perpendicular to the optical axis against two retainer pads located with a separation of 90°. The lens mounts were fabricated after the lens dimensions became available. The lens mounts were designed for the lenses to be located at the correct position when they are cooled. Since the lens heights are different in each lens at room temperature, due to different physical sizes and differential thermal contraction, we measured and adjusted the position of the lens mounts using an alignment telescope. The plate springs were designed to hold at least twice the gravitational force of each lens in each direction. The stress induced in the lenses at 77 K was calculated both analytically and by a simulation with a finite element method. We confirmed that such induced stresses are too light to damage the lenses in their mount.

3.2. *Mechanical Structure*

MOIRCS has three main structures, as shown in figure 6: the main cryostat, the MOS system, and the support structure. The main cryostat consists of several short aluminum cylinders and plates for easy fabrication and cost reductions. They were connected and sealed using Viton O-rings for a vacuum. There are four kinds of support structures, which are called top ring, delta wings, supporting arms, and supporting legs, respectively. They are all made of aluminum. The top ring is a mounting structure of the MOIRCS to the telescope, and hence defines a reference to MOIRCS. All other structures are directly connected to the top ring to prevent interferences with each other. The delta wings support the main cryostat near its center of gravity to minimize any flexure. Supporting arms

were added to assist the delta wings, because the center of gravity turned out to be slightly under the points where the delta wings support the main cryostat. The supporting legs carry auxiliary items, such as PCs, a vacuum pump, and motor drivers.

Inside the main cryostat, the optical-bench plate is supported by thick G10 straps from the wall of the cryostat in both the vertical and horizontal directions (see figure 1). The optical-bench plate has side walls in both the collimator and the camera sections, and two bulkheads between the two sections for reinforcement. The two bulkheads support the shafts of the filter turrets and their compartment.

We performed a finite element analysis of the structure, and confirmed that the flexure of the instrument at any instrument orientation, i.e., telescope elevation and instrument rotator angle, is smaller than 200 μm, which does not affect the optical performance and is required to keep observing objects on the slits for at least two hr during MOS observations.

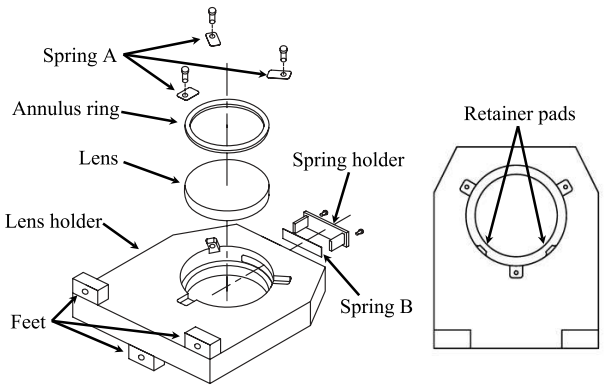

Fig. 5. Schematic drawing of the lens mount. (Copyright SPIE [2003].)

3.3. *Cooling System*

In order to reduce thermal radiation from the instrument, itself, almost all items in the cryostat have to be cooled to at least 150 K. Since the heat capacity of the internal mass is very large, we use a liquid nitrogen precooling system to cool it to an operational temperature within a specified time, and a mechanical cooler to keep the cold temperature. We chose one of the most powerful (35 W at 45 K for the first stage and 6.3 W for the second stage) 2-stage mechanical coolers available. The first stage, which is connected to the optical-bench plate, is powerful enough to maintain a temperature of $\sim$100 K, while the second stage keeps the temperature of the FPAs and the detector modules at 77 K with some extra power. Regard was paid to the fact that the same model of mechanical coolers has been used for several other Subaru instruments, from the point of view of maintenance. Copper straps and wires are used to connect the cold heads with the optical-bench plate and the detector modules. The FPA is cooled via grid pins on the ceramic package, which are not wired into the FPA. A copper plate, which is soldered to the pins of zero insertion force (ZIF) socket, is used as a heat reservoir. Two small surface-mount type Pt resistors are also soldered to the ZIF socket pins as temperature sensors. In the precooling system we use copper tubings silver-soldered to copper plates, which are attached to the optical-bench plate for heat exchange, and use steel bellow tubings connecting the copper plates with the ports on the cryostat wall (figure 7). We have not adopted conventional hard radiation shields, because of the complex shape of the cryostat and the optical-bench plate. Instead, the optical-bench plate is wrapped with a multi-layer insulation (MLI) jacket to prevent thermal radiation through the wall of the cryostat (figure 7). Based on calculations of the thermal conduction and radiation,

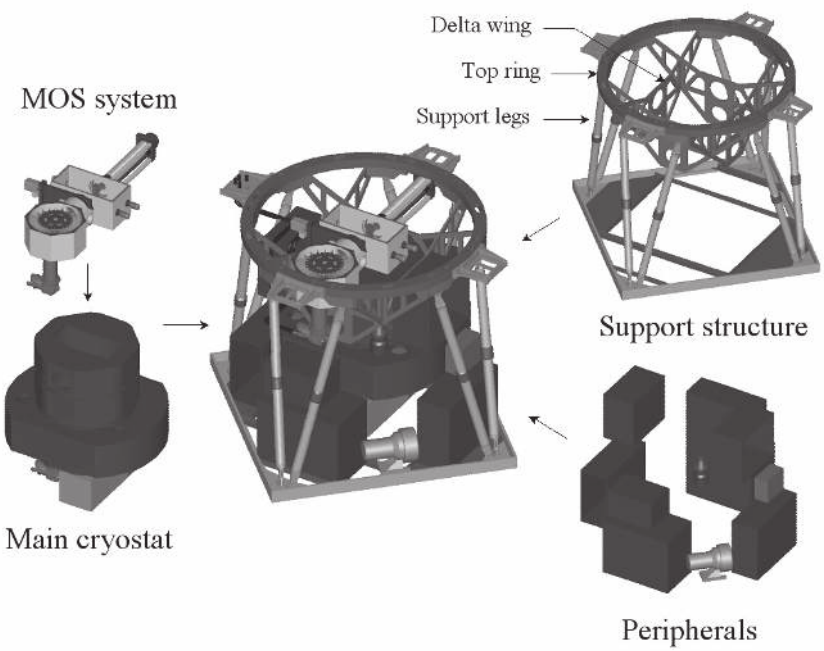

Fig. 6. Overall structure of MOIRCS.

Fig. 7. Precooling system (left) and optical-bench plate covered by MLIs (right). (Copyright SPIE [2006].)

we use ten layers of MLI, all of which consist of a thin aluminum coated polyester (9 μm) and a thin polyester net (200 μm) as a spacer. Because the lenses used in MOIRCS are large, the cooling rate is controlled at a rate of less than 5 K h^{-1} during precooling to prevent damage from thermal shock or stress caused by rapid contraction of the aluminum lens mounts.

3.4. House Keeping

The house keeping electronics are necessary to operate MOIRCS, and to monitor its status. They include cryogenic stepper motors and their drivers, pneumatic actuators for the MOS system, temperature sensors, heaters and their controllers, vacuum gauges, data-handling electronics for various sensors, and power distributors. Most of them were chosen from the observatory standards, because of maintenance advantages. A schematic diagram of MOIRCS electronics components is shown in figure 8. As we describe in subsection 3.7, we adopted TCP/IP as a communication protocol between the host Linux PCs and each device, and distributed all devices in a local area network. Devices controlled by a serial connection, such as RS232C, are connected to the network via a TCP/IP-to-RS232C converter.

3.5. Cryogenic Mechanical Components

MOIRCS has three cryogenic mechanical components: filter turrets, focus stages, and the slit mask exchanger system. The filter turrets adopt the Geneva mechanism for intermittent moving and are driven by cryogenic stepper motors. Ball bearings that are commercially available and are made of stainless steel with a certain type of retainer were selected in consultation with the manufacturer. The focus stages have ball screws and linear slides, which are also made of stainless steel and are driven by cryogenic stepper motors. The bearings and linear slides were all degreased. For the filter turrets and the focus stages we used magnets and InSb Hall effect sensors for accurate positioning. They are used to define the home position of the filter turrets and to measure the position of the focus stages. The magnets are glued onto the moving side (i.e., turret wheel and detector housing), while the sensors are glued onto the stationary side (i.e., turret cover and detector mount) with a narrow gap with the magnets. The magnets are set up so that the magnetic field moves across the Hall effect sensor. The Hall effect sensors used are commercially available, and are not specified for cryogenic use. However, we confirmed that the position is detected down to an accuracy of 10 μm, and linearity is kept at 77 K in the range of our interests ($\pm$ 1 mm for the focus stage). The output of the Hall effect sensors are

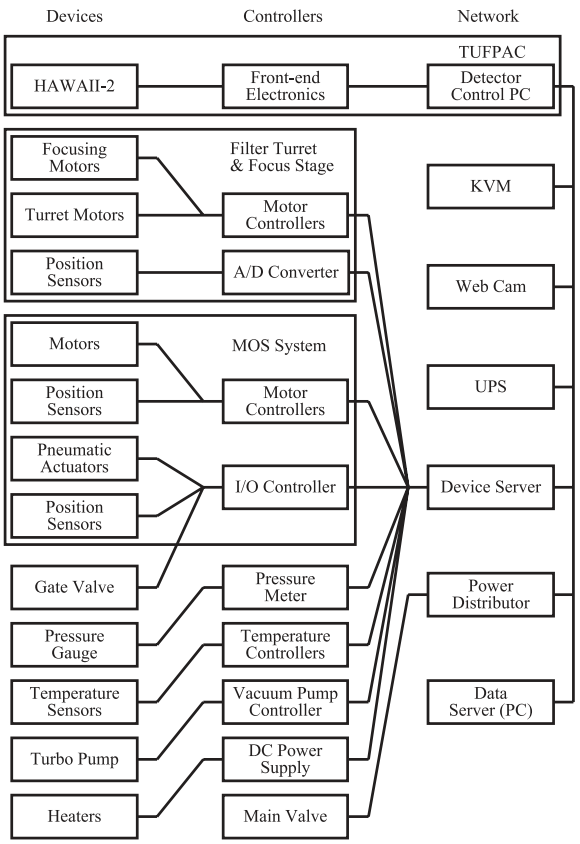

Fig. 8. Schematic diagram of the electronics components.

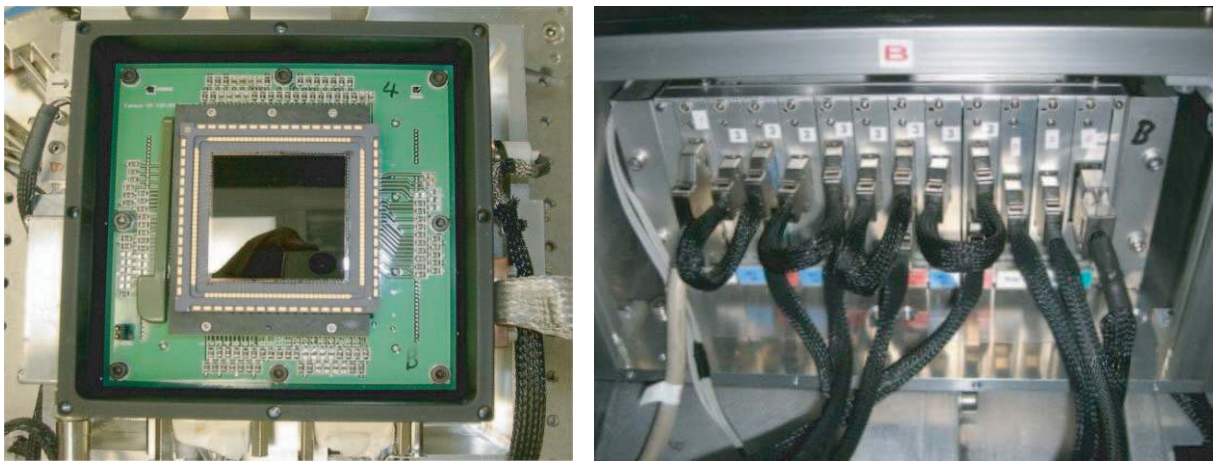

Fig. 9. HAWAII-2 FPA mounted on the detector module (left) and front-end electronics of TUFPAC (right). (Copyright SPIE [2006].)

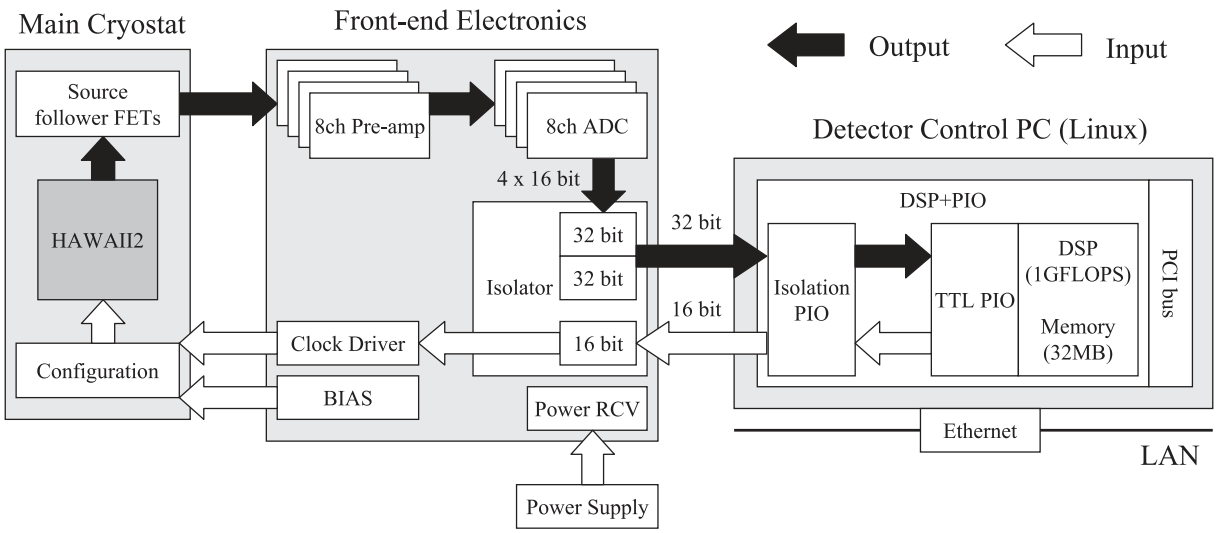

Fig. 10. Data-acquisition flow of TUFPAC.

amplified and digitized by commercially available I/O modules and monitored by a PC every 100 ms. Operating the cryogenic stepper motors and reading the output of the Hall effect sensors are independent of each other, except in a home-positioning process of the filter turrets. When the filter turrets are sent to their home positions, the output of the Hall effect sensors are sent to the comparators that sense the threshold voltage, and the trigger signals from the comparators are fed into motor drivers to stop the turrets.

3.6. Detector Control

As the format of FPAs becomes larger, fast and efficient acquisition of FPA data at the low-noise level is more critical for astronomical instruments. When we started designing MOIRCS, suitable FPA controllers were not commercially available from any vendor. These facts led us to develop our own FPA control system, TUFPAC (Tohoku University Focal Plane Array Controller: Ichikawa et al. 2003), for flexible control of the HAWAII-2 FPA and fast and efficient acquisition of the image data (figure 9). Although the system was originally designed especially for the HAWAII-2 FPA, it turns out to be applicable to optical CCDs with minor changes of the front-end electronics. For setting up the system we used as many as possible components commercially available for purposes of low cost and less maintenance.

Figure 10 shows the schematic configuration of TUFPAC along with the signal and data flow. TUFPAC consists of a Linux PC with a commercially available digital signal processor (DSP) board on a PCI bus, front-end electronics to the HAWAII-2 FPA, and linear power supplies. DSP is one of the methods used to realize real-time operation of FPAs, which is essential for astronomical applications. The DSP board with a 1 GFLOPS DSP and a 32 MB RAM memory can communicate with the front-end electronics without any interruption from the host PC, i.e., sending clock signals to and receiving image data from the front-end electronics based on codes stored in memory. The DSP programs, written in C, are compiled to the DSP codes and transferred to the DSP

memory. The DSP of 1 GFLOPS is fast enough for calculations or image processing in the memory, and the 32 MB memory is large enough for frame data of 16 MB each. Since the DSP board can handle an optional TTL parallel I/O (PIO) board with 32-bit inputs and 32-bit outputs, an isolation PIO board using photocouplers is designed to isolate the front-end electronics, which is more sensitive to electric noise from the DSP board. We use 16-bit outputs of TTL PIO board for controlling the HAWAII-2 FPA and 32-bit inputs for receiving the data from two AD converters (ADCs) simultaneously.

The front-end electronics is comprised of a power-receiving board, an isolation board, a bias board, a clock driver board, four 8-channel preamplifier boards, and four 8-channel ADC boards. All boards are based on VME-3U size cards and housed in a single rack outside the main cryostat (figure 9). DC voltages from the linear power supplies are cleaned by low-pass filters on the power-receiving board and fed to the other boards via the backplane buses of the rack. The isolation board, which is a counterpart of the isolation PIO on the PCI bus of the host Linux PC, isolates the front-end electronics electronically from the DSP boards. The bias board and the clock driver board create precise biases and clocks that are necessary for the HAWAII-2 FPA. The preamplifier board and the ADC board amplify and digitize FPA data, respectively. Wiring between the boards is through the backplane buses.

Inside the main cryostat, HAWAII-2 FPA is mounted on a ZIF socket which sits on the top of two stacked circuit boards where the biases and clocks from the front-end electronics are distributed to four quadrants of the HAWAII-2 FPA, and the output data from the FPA are amplified by source follower FETs. The external source follower FETs are available in place of built-in FETs on the HAWAII-2 FPA to eliminate the glow, as proven on HAWAII FPA (Motohara et al. 2002). The wirings between the FPA and the front-end electronics are carefully done to avoid electromagnetic interference by other electronic devices.

Data-acquisition flow using TUFPAC is shown in figure 10. When an exposure starts, the Linux PCs are prompted by a parent workstation that manages the entire observation sequences. The PCs then send a program for reading the FPA to the DSP boards, which supply clock patterns to the front-end electronics. The front-end electronics converts the clock patterns from the DSP boards to powers, biases, and clocks needed for the FPA. The data from the FPA are amplified and digitized by the front-end electronics, sent back to the DSP boards, and stored in the RAM memory. At the end of the exposure, the same sequence is repeated, and the difference between the two becomes the final data for one exposure. The data stored in the memory on the DSP boards can be processed if necessary (e.g., coadding). The final data are transferred to the Linux PCs and converted as frame data in the FITS format.

The HAWAII-2 FPA has 4- and 32-output readout modes. TUFPAC can handle both readout modes without any hardware changes. It takes 11.5 and 1.4 s to read all of the pixels in the 4- and 32-output readout modes, respectively. TUFPAC can also handle a partial readout for observations of bright objects, like standard stars. Using the partial readout mode, for example, we can read a central 512×512 pixels area in 1 s.

3.7. Software

Important roles of an integrated control software system are to control the devices, to manage the status of the devices, and to provide an interface to users (observers, instrument operators, or developers). A large number of configuration parameters (~ 150) and status data (~ 120) are necessary for observations with MOIRCS and Subaru Telescope. The data are added or deleted during instrument development, or maintenance such as filter exchange. In addition, because the software has been developed in parallel to the hardware development, a wide range of flexibility is needed to accommodate various kinds of devices, various types of experiments, and even different developers who use different programming languages. To manage these complex, but not unusual, situations in the instrument development, we developed a simple and flexible integrated software called T-LECS (Tohoku University - Layered Electronics Control System: Yoshikawa et al. 2006).

Figure 11 shows a schematic diagram of T-LECS. There are three layers defined in the T-LECS: an external layer, an internal layer, and a communication layer. The external layer has two user interfaces: one is for upper-level observation software system, which is the Subaru Observation Software System (SOSS: Kosugi et al. 1997), and the other is for the instrument developer or operator who wants to access to the devices directly. The internal layer is joined to each terminal device, which is mentioned in subsection 3.4. The communication layer holds any kind of system data, such as configuration information of removable components in the instrument, device status information, and FITS header information. We use a relational database system to handle all of the data easily and efficiently. The external and internal layers are joined to their clients using specific languages that are comprehensible to them. Translation from one language into another is an important function of the communication layer. For example, a "*J* band filter" in the external layer is translated into "the second slot of the first turret" in the internal layer.

A relational database has been used in other software systems for astronomical applications. For example, Clarke and Allen (2000) generates source codes, documents, and GUI applications using system configuration data in the relational database. Our approach, on the other hand, uses the relational database in real time during observations, and not only the configuration data, but also the status data and FITS header data are handled by the relational database.

Because some processes, such as detector readout and data reduction for a quick look, are heavy CPU consumers, which might affect the rest of the system, we distribute all processes to the four PCs according to their loads and their hardware connections. In order to achieve flexible process allocation, TCP/IP is used for interprocess communication, such as command communication and status query, and the four PCs are placed in the local area network. Because the relational database server is also accessible from the network, any process can be issued from any PC in the network using the data in the relational database server. Another advantage of adopting the TCP/IP protocol is that the serial terminal devices can be placed anywhere in the local area network without being limited by the physical cable length through the use of

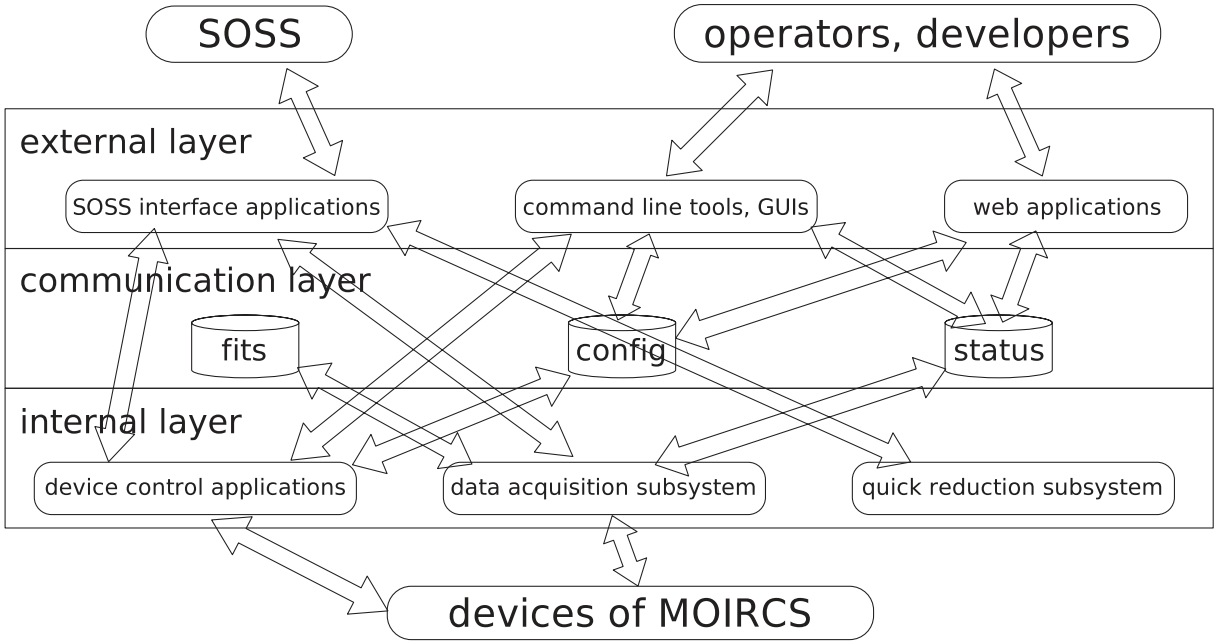

Fig. 11. Schematic diagram of T-LECS. Arrows indicate communications between individual functions. (Copyright SPIE [2006].)

a TCP/IP-to-RS232C converter.

We make T-LECS libraries with an object-oriented scheme to make developments of new applications easier. The library is divided into packages, which are groups of fundamental functions for specific instrument features. We can code using the functions in the packages when we add a new application to T-LECS. The libraries can be converted to those with different programming languages in the same scheme. For example, some of the web applications for MOIRCS are created by using the T-LECS library ported to PHP.

4. Performance

In this section, we describe detector performances in subsections 4.1–4.7, imaging performances in subsections 4.8–4.10, and system performances in subsections 4.11–4.14. All of the performances shown here are based on data obtained through laboratory tests and from commissioning observations.

4.1. Conversion Factor

The conversion factor, g (e^- ADU^{-1}), of the FPA and the electronics is calculated by a least-squares fitting using

$$N_{\rm total}^2 = N_{\rm read}^2 + \frac{S}{g}, \tag{1}$$

where $N_{\rm total}$ is the total noise, $N_{\rm read}$ the readout noise, and S the signal, all in units of ADU. We use a warm aluminum plate attached just above the entrance window of the cryostat as a light source in the $K_{\rm s}$ band. Twenty frames are taken for each of twenty different exposure times to obtain S and $N_{\rm total}$. The calculated conversion factors are 3.15 and 2.86 e^- ADU^{-1} in Channel 1 and Channel 2 of the two optical channels, respectively.

4.2. Dark Current

The dark current is measured by taking images of a cold blank plate (100 K) with different exposure times. We obtain 0.080 e^- s^{-1} in both channels. The dark current is small enough for the normal background limited imaging observations. However, we note that the dark current of the HAWAII-2 FPAs used in MOIRCS depends on the pixel counts of the previous image; the more the pixel counts are, the higher the dark current in subsequent images is. The phenomenon is called "excess dark current" or "persistence", which was observed in some HAWAII FPAs (Hodapp et al. 1996; Finger et al. 1998; Motohara et al. 2002). As the excess dark current decreases with time, care should be taken, after background brightness changes, the filter is changed, or the observation mode is changed. It takes 40 min for the dark current to come back to the normal value if the FPAs are continuously read after they are completely saturated.

4.3. Readout Noise

Readout noise is measured by using the dark frames with the shortest exposure time in which the dark current is negligible. We obtain 31 e^- rms in both channels with a correlated double sampling (CDS) readout method when MOIRCS is mounted at the Cassegrain focus of the Subaru Telescope. Since a laboratory test gave 17 e^- rms, the house-keeping components in the MOIRCS package possibly generate systematic noises. In fact, multisampling with 16 readouts gives 15 e^- rms, which does not obey the law of statistics that the random noise decreases with $N^{-\frac{1}{2}}$, where N is the number of sampling. The readout noise, however, is small enough for normal background-limited imaging observations.

4.4. Linearity and Full Well

Because most of other near-infrared instruments have not any shutter and neither has MOIRCS, the exposure time is controlled by the readout timing. Therefore, the full well and the count under which linearity stays within a usable range vary, depending on each pixel location and the amount of input flux. Because it takes 11.5 s to read an entire quadrant and the last pixel is exposed to the input flux longer than the earlier pixels before it is read out, the minimum full well, which we always want to keep the count smaller than, happens at the last pixel. The relation between the input flux and the minimum full well follows a simple equation,

$$C_{\rm CDS} = C_{\rm single} - F t_{\rm r}, \quad (2)$$

where $C_{\rm CDS}$ is the minimum full well with the CDS method in units of e^-, $C_{\rm single}$ the full well with a single sampling method in units of e^-, F the input flux in $e^-\,{\rm s}^{-1}$, and $t_{\rm r}$ time to read out the entire quadrant (11.5 s).

The linearity and the minimum full well of the HAWAII-2 FPAs are calculated from the same data set used for the conversion factor described in subsection 4.1. The measurements are done with the CDS method, and the results are translated into the values with the single sampling method. We find that the full wells are $\sim 154000\,e^-$ and $\sim 138000\,e^-$, and the linearities are kept within 3% to $\sim 94000\,e^-$ and $\sim 115000\,e^-$ for the single sampling method in Channel 1 and Channel 2, respectively.

4.5. Quantum Efficiency and Cosmetics

Figure 12 shows histograms of the quantum efficiency in the J, H, and $K_{\rm s}$ bands. Figure 12 was derived from count histograms of flat field images by scaling median values to the quantum efficiencies provided by the vendor. The quantum efficiencies of the HAWAII-2 FPAs in Channel 1 and Channel 2 are 0.717 and 0.628 in the J band, 0.705 and 0.867 in the H band, and 0.658 and 0.833 in the $K_{\rm s}$ band, respectively. Figure 13 shows flat field images in the $K_{\rm s}$ band as an example of the quantum efficiency distribution and the cosmetics of the HAWAII-2 FPAs.

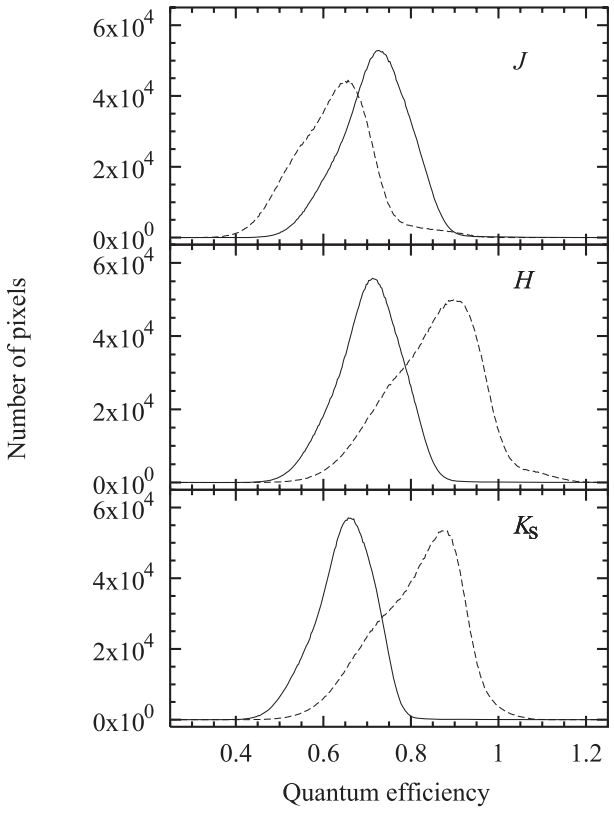

Fig. 12. Histograms of the quantum efficiency in the J, H, and $K_{\rm s}$ bands. The solid and dotted lines indicate Channel 1 and Channel 2, respectively.

4.6. Reset Anomaly

We have observed a tilt of the detector bias, which is called a "reset anomaly" or a "bias tilt" (Kozlowski et al. 1994; Finger et al. 2000; Yanagisawa et al. 2006). The tilt appears along a slow read direction in both the 4- and 32-output readout modes. The reset anomaly is seen in some HgCdTe FPAs, such as HAWAII and HAWAII-2, and its strength is different for individual FPAs. For the HAWAII-2 FPAs used in MOIRCS, the reset anomaly is reduced and stabilized by operating them continuously, and is well subtracted by the CDS method. In order to evaluate the reset anomaly, ten consecutive dark frames are taken, and each quadrant area is averaged in a fast read direction. The peak-to-valley values of the reset anomaly in the dark frames are less than $12\,e^-$, and are stable within $1\,e^-$. Although the effect of the reset anomaly depends on the type of observation, it is negligible in the normal background-limited imaging observations, for example, for studying high redshift galaxies. However, if observers want to reduce the reset anomaly further, they may use the following option: send the same clock pulses as the readout just before each of the two actual readouts of the CDS method (i.e., reset – read clock – read – exposure – read clock – read). The reset anomaly will be reduced, but the trade-off is that the minimum exposure time becomes 20.5 s for the full readout in the 4-output readout mode.

4.7. Readout Modes

We have started MOIRCS operation with the 4-output readout mode with the built-in FETs as the simplest readout mode. However, the long readout time of 11.5 s gives a large overhead, typically 40% for imaging in the $K_{\rm s}$ band, and even higher in the H band under high sky background. On the other hand, for spectroscopic observations or imaging with narrow-band filters with very low sky background, the glow of the built-in FETs is a major source of noise. In particular, for readout with multiple sampling, which is common in low-background observations, the effect is serious (when the MOIRCS arrays were procured, HAWAII-2RG with negligible glow was not available). Experiencing these problems, we have tried the 32-output readout mode with the off-chip source follower FETs instead of the built-in FETs. The configuration succeeds to reduce the glow considerably (see figure 14). However, strong crosstalk occurs with the 32-output readout mode, while no crosstalk is seen with 4-output readout mode.

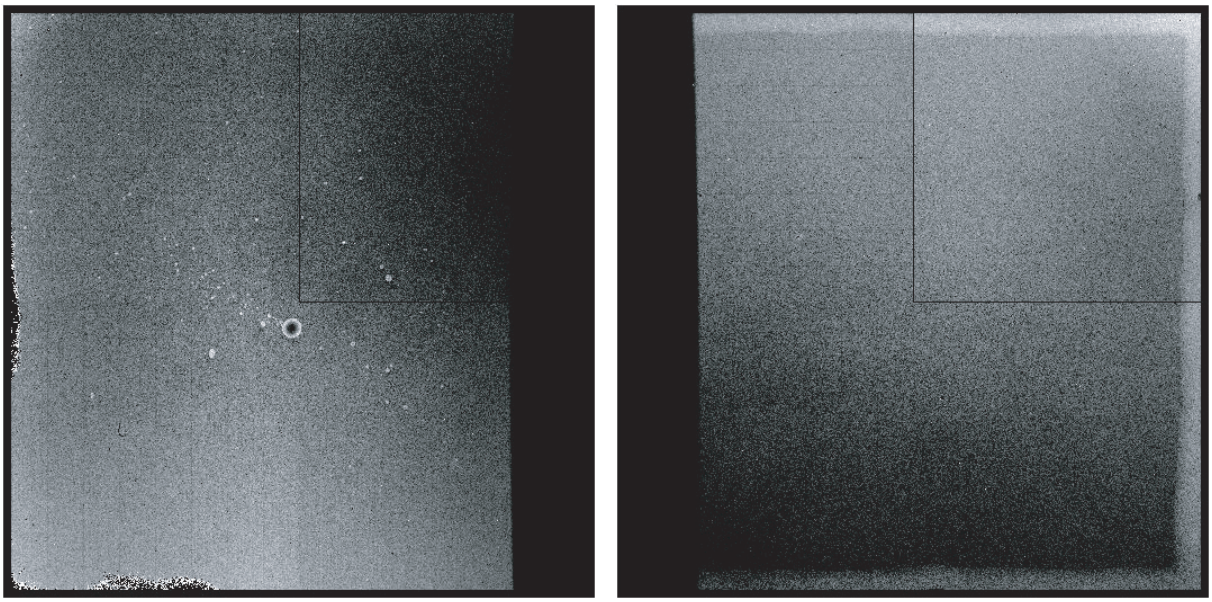

Fig. 13. Flat field frames of Channel 1 (left) and Channel 2 (right).

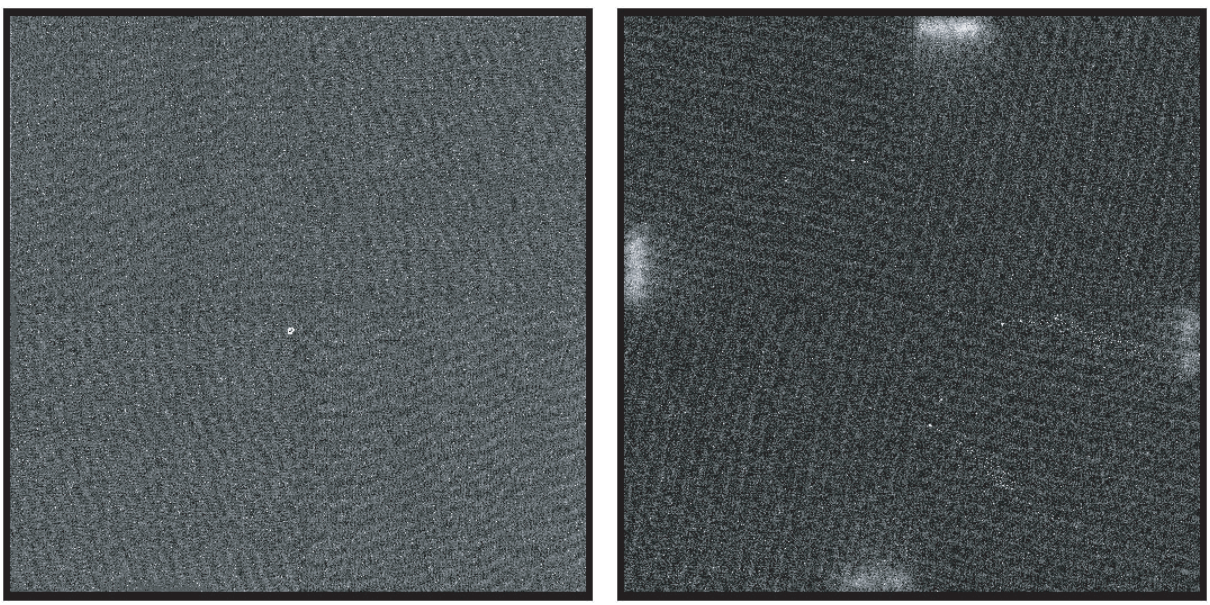

Fig. 14. Dark frames of Channel 1 (left) and Channel 2 (right).

Since the origin of the crosstalk is not known yet, we usually choose the 4-output readout mode at the cost of observation efficiency.

4.8. Image Quality

The image quality is evaluated by taking images of a star field, where adequately bright stars are distributed over a FOV as uniformly as possible, under conditions of good seeing at various focus positions of the telescope. We pick up only bright stars with a good S/N ratio, and calculate the FWHMs of their flux profiles using SExtractor (Bertin & Arnouts 1996). Figure 15 shows FWHM distributions along each image axis at various focus positions of the telescope. The best image quality is obtained at the same telescope focus ($z = 0.175$) in both channels, and the best FWHM (~ 2.5 pixels) is kept over the FOV with a peak-to-valley variation of less than 1 pixel. Less peak-to-valley variation could be obtained with finer focus intervals of the telescope. The FWHM variation is hardly perceivable with an average seeing condition in the K_s band ($\sim 0''.5$).

On the other hand, the smallest FWHM obtained so far is 1.5 pixels in the K_s band, which corresponds to $0''.18$ on the sky. The results demonstrate that MOIRCS can definitely take advantage of the excellent seeing on Mauna Kea.

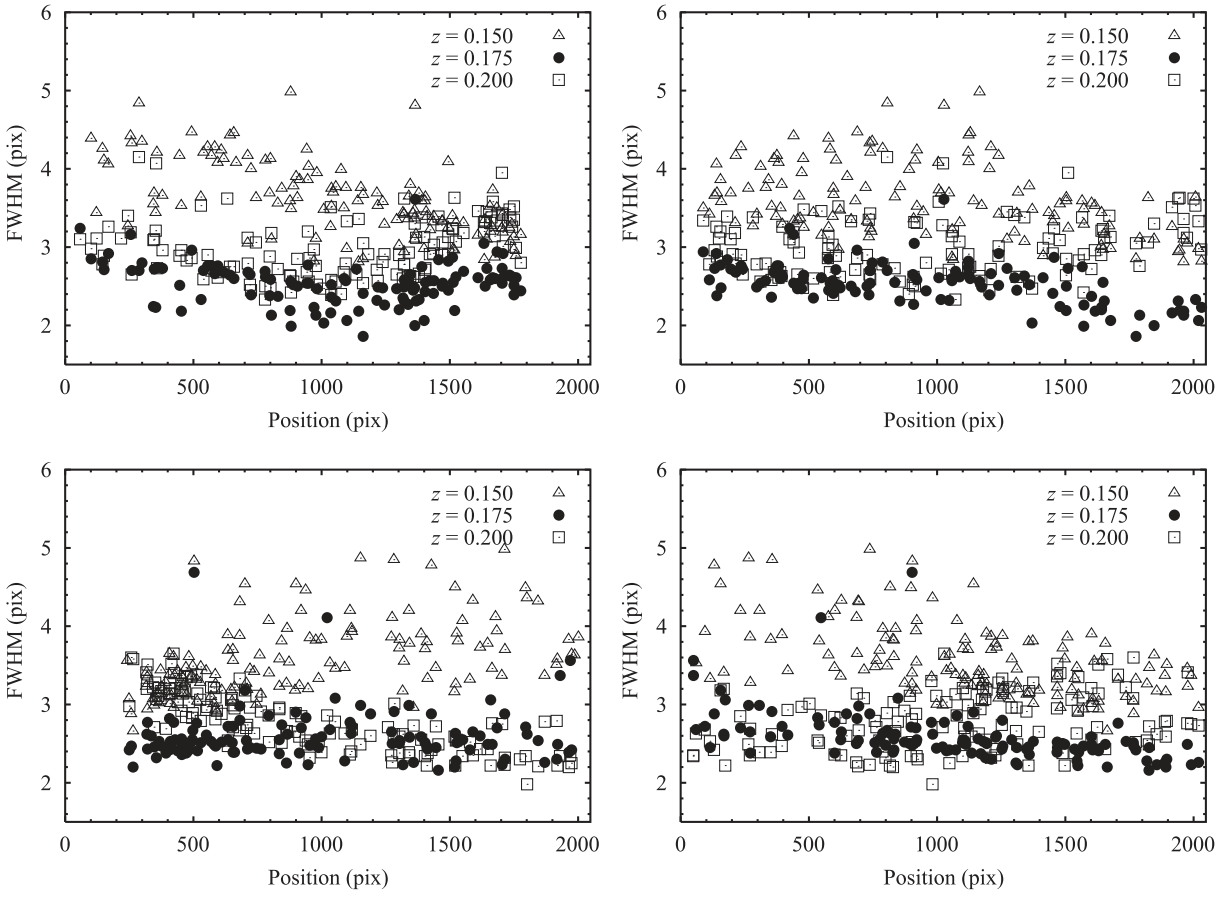

Fig. 15. Distributions of the FWHMs of stellar objects along a horizontal axis (left) and a vertical axis (right) in the images of Channel 1 (top) and Channel 2 (bottom). Different focus positions of the telescope (z) are expressed by different symbols. Filled circles indicate the best focus position. Data with larger FWHM than 5 pixels are not shown for a visual purpose.

4.9. Distortion Correction

We derived the distortion correction function using stellar objects that are commonly detected both in a Subaru Prime Focus Camera (Suprime-Cam: Miyazaki et al. 2002) image and in a MOIRCS image. The Suprime-Cam image is a good reference for this purpose, because (1) it has a much larger FOV (30′ in diameter) than MOIRCS, which eliminates any uncertainty caused by mosaicking small reference images, (2) it has celestial objects with proper magnitude for MOIRCS, and (3) its distortion is well corrected (Miyazaki et al. 2002). The coordinates of the stellar objects in both images are compared and fitted using third-order polynomials with a Seidel's distortion coefficient, scale factor, rotation, translation of the images, and coordinates of the optical axis. Figure 16 compares the derived distortion with that of the design. The distortion is 2% at the edge of the images, agreeing well with the design. The positional accuracy of the distortion-corrected coordinates is 0.3 pixels (0.″04) (rms).

4.10. Chromatic Aberration

We evaluate the lateral chromatic aberration by comparing the coordinates of stellar objects in star-field images taken sequentially with different filters. Any distortion is corrected using the distortion correction function described in subsection 4.9. The results are summarized in table 3 with the J band image as a reference. The maximum difference of magnification (column 3) is 0.017% between the J and K_s bands in Channel 2, which corresponds to 0.25 pixels (0.″030) at the edge of the FPA (column 4). The results agree with the design value of 5 μm (0.28 pixels).

The axial chromatic aberration is evaluated by placing a slit mask with a pinhole grid on the Cassegrain focal plane and locating the best focus position for each filter while moving the focus stage along the optical axis. Because the pinhole size is 80 μm in diameter which corresponds to 1.4 pixels at the FPA, the chromatic aberration is evaluated with sufficient accuracy. The results are also summarized in column 5 of table 3. The maximum axial chromatic aberration of 29 μm agrees well with the design value of 40 μm. Because we cannot see image degradation in the J, H, and K_s band images at the same detector position, the chromatic aberration has negligible impact.

4.11. Mosaic of Images

MOIRCS creates two separate FITS images for one exposure, corresponding to the two FPAs. They can be mosaicked together using a set of geometrical rules derived from

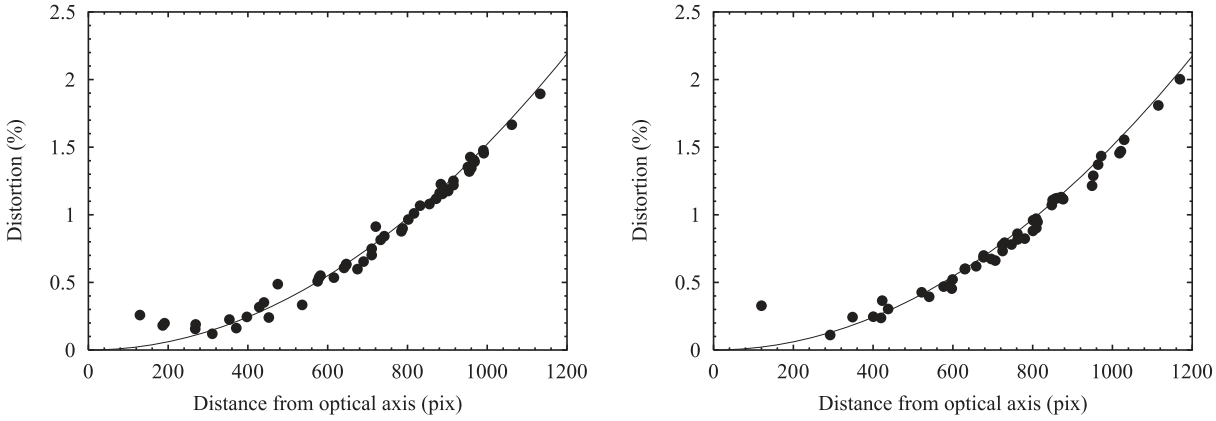

Fig. 16. Distortions of MOIRCS images in Channel 1 (left) and Channel 2 (right). Filled circles are measurements, while solid lines show the expected distortion from the design.

Table 3. Summary of chromatic aberrations.

	Filter	Lateral (%)	Lateral (pixel)*	Axial (μm)
Channel 1	J	—	—	—
	H	1.0×10^{-2}	0.14	−9
	$K_{\rm s}$	6.7×10^{-3}	0.10	−9
Channel 2	J	—	—	—
	H	1.2×10^{-2}	0.17	29
	$K_{\rm s}$	1.7×10^{-2}	0.25	25

* Maximum chromatic aberration at the edge of image.

observation. However, because the rules are not always the same, due to instrument flexure and a slight play of the optics or the detector, we evaluate the accuracy of the relative alignment of the two images.

We take an image of the pinhole grid placed at the Cassegrain focal plane at various instrument orientations. Geometrical rules established at the zenith position are applied to all of the images for mosaicking. Figure 17 shows how the relative coordinates of the pinhole grid in Channel 2 against Channel 1 change with the orientations. A systematic shift toward the $+X$ direction seen in figure 17 can be explained by a shift of the lenses in the direction of gravity. The elliptical motion with the image rotator angles can be explained by a shift of the FPAs. The accuracy of the relative alignment of the two images is found to be $\pm\,1$ pixel ($\pm\,0\farcs1$) if predetermined geometrical rules are applied. However, if we derive the geometrical rules at the same instrument orientation during an observation, the alignment can be corrected to a level of 0.3 pixels ($0\farcs04$) (rms). This can be done by offsetting the field in order to relate objects detected in each of the original two images within one image of the offset field.

4.12. *Throughput*

Throughput is defined as

$$\gamma = \frac{C_{\rm obj}\, g}{F_{\lambda,{\rm obj}} A_{\rm tel} \Delta\lambda}, \tag{3}$$

where $C_{\rm obj}$ is the count rate of an object in ADU s^{-1}, g the conversion factor in e^- ADU^{-1}, $F_{\lambda,{\rm obj}}$ the photon flux of the object in photon s^{-1} cm^{-2} μm^{-1}, $A_{\rm tel}$ the effective area of the telescope in cm^2, and $\Delta\lambda$ the passband width of a filter in μm. The throughput is the fraction of photons collected by telescope from an object within the wavelength range $\Delta\lambda$ that change to electrons at the FPA. We measure the count rates of the UKIRT standard stars (Hawarden et al. 2001) on different dates and with different air masses to derive the throughput for objects at the zenith. The measured throughputs are 0.23 and 0.23 in the J band, 0.34 and 0.34 in the H band, and 0.28 and 0.32 in the $K_{\rm s}$ band in Channel 1 and Channel 2, respectively (the results are also summarized in table 4). The throughputs agree well with those expected in the H and $K_{\rm s}$ bands in Channel 1, but all others are 10%–25% less than the expectations. The cause of the degradation in the throughput is not yet clear.

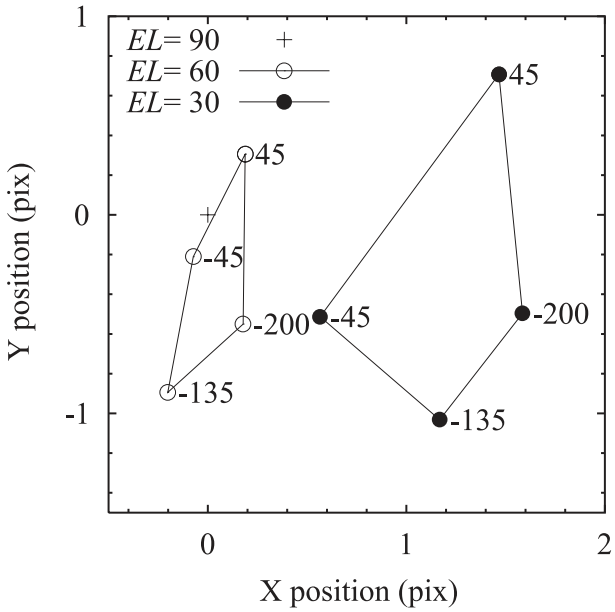

Fig. 17. Relative coordinates of the pinhole grid in Channel 2 against Channel 1. The cross, open circles, and filled circles indicate elevation angles of 90° (zenith), 60°, and 30°, respectively. Figures near the symbols mean instrument rotator angles in degree.

Table 4. Performance summary of MOIRCS.

Readout noise	$31\,e^-$
Dark current	$0.080\,e^-\,\mathrm{s}^{-1}$
Resolution of point source	FWHM $< 0\farcs18$
Image quality	Degradation hardly perceivable in an average seeing condition.
Chromatic aberration	$0\farcs030$ at the edge of image (lateral). Hardly perceivable (axial).
Distortion	2% at the edge of image. Correction accuracy is $0\farcs035$ (rms).
Mosaic accuracy	$\pm0\farcs1$ at maximum. Accuracy can be improved to $0\farcs04$ (rms) (see text).
Throughput*	0.23/0.23 (J), 0.34/0.34 (H), 0.28/0.32 (K_s)
Background brightness†	$15.6^{+0.9}_{-0.5}$ (J), $13.9^{+0.8}_{-0.5}$ (H), $13.8^{+0.4}_{-0.3}$ (K_s) mag arcsec^{-2}
Limiting magnitude‡	23.7 (J), 23.0 (H), 22.6 (K_s) mag

* Throughput (Channel 1/Channel 2) includes the instrument, the telescope, and the atmospheric transmission at zenith.
† Background brightness with 1σ variation.
‡ One hour exposure, $S/N = 5$, point source with $0\farcs5$ seeing, and $1\farcs0$ aperture.

4.13. Background Brightness

The background brightness is defined as

$$m_\mathrm{bg} = -2.5\log\left(\frac{C_\mathrm{bg} g\gamma hc}{A_\mathrm{tel}\lambda\Delta\lambda\theta^2}\right) + m_0 - 10, \quad (4)$$

where C_bg is the count rate of background regions in ADU s^{-1}, g the conversion factor in e^- ADU^{-1}, γ the throughput obtained in subsection 4.12, h the Plank constant in erg s, c the light velocity in cm s^{-1}, λ the center wavelength of the filter transmission in μm, θ the pixel scale in arcsec pixel^{-1}, and m_0 the zero point of the Vega magnitude calculated from the throughput obtained in subsection 4.12. We only use images taken between 9:00 p.m. and 3:00 a.m. from April to November in 2006. The measured median background brightness are 15.6 mag arcsec^{-2} in the J band, 13.9 mag arcsec^{-2} in the H band, and 13.8 mag arcsec^{-2} in the K_s band (see 1σ fluctuation in table 4). However, we note that the background brightness in the near-infrared region changes drastically, not only from day to day, but also in one night, especially in the J and H bands, as shown in Labbé et al. (2003).

4.14. Limiting Magnitude

We calculate the limiting magnitude for all photometric bands using the measured background brightness and the throughput. The estimated limiting magnitudes for a point source are 23.7 in the J band, 23.0 in the H band, and 22.6 in the K_s band with $S/N = 5$, $0\farcs5$ seeing, $1\farcs0$ aperture, and a 1 hr exposure (table 4). The limiting magnitudes are slightly deeper than those of CISCO, due to the lower level of the OH airglow background brightness in the J and H bands measured by MOIRCS, compared to that of CISCO, while we cannot compare the limiting magnitude in the K_s band because CISCO uses the K' band (Motohara et al. 2002). However, we note that the actual limiting magnitude may be slightly different from that estimated due to correlation noises generated during the reduction process, or undetected faint sources, as pointed out by Labbé et al. (2003).

5. Summary

We have developed the near-infrared camera and multi-object spectrograph MOIRCS for the 8.2 m Subaru Telescope. MOIRCS provides imaging for the $4' \times 7'$ FOV with a pixel scale of $0\farcs117$ pixel^{-1}, and MOS capability in the wavelength range of 0.85 to 2.5 μm. The details of the optics, electronics, software, structure design, house keeping system, and cooling system are described in this paper. The imaging performances, the detector performances, and the system performances evaluated based on the data obtained through the laboratory tests and the commissioning observations are found to reach the design goals, and are good enough for normal background-limited observations. MOIRCS is now available for open use, and is expected to be used in many astronomical fields.

We would like to thank the Subaru Telescope Directors during the MOIRCS project period for their support. We thank N. Kobayashi for his continuous advices through the development. We thank K. Asai, D. Matsumoto, and K. Yanagisawa for their contributions in the early stage of the project. We also thank K. Martin for assisting the mechanical design, D. Jackson, B. Elms, and all the people in the machine shop at Tohoku University for precise machining, and B. Piccirillo, who provided high-quality optics for MOIRCS. Finally, we thank all staff members of the Subaru Telescope for supporting us in every aspect of the project. This research is supported in part by Grants-in-Aid Scientific Research (11554005 and 14340059) of the Ministry of Education, Culture, Sports, Science and Technology. The Image Reduction and Analysis Facility (IRAF) used in this paper is distributed by the National Optical Astronomy Observatories, which are operated by the Association of Universities for Research in Astronomy, Inc., under cooperative agreement with the National Science Foundation.

References

Bertin, E., & Arnouts, S. 1996, A&AS, 117, 393
Clarke, D. A., & Allen, S. L. 2000, APS Conf. Ser., 216, 16
Cuby, J.-G., Hibon, P., Lidman, C., Le Fèvre, O., Gilmozzi, R., Moorwood, A., & van der Werf, P. 2007, A&A, 461, 911
Daddi, E., Cimatti, A., Pozzetti, L., Hoekstra, H., Röttgering, H. J. A., Renzini, A., Zamorani, G., & Mannucci, F. 2000, A&A, 361, 535
Daddi, E., Cimatti, A., Renzini, A., Fontana, A., Mignoli, M., Pozzetti, L., Tozzi, P., & Zamorani, G. 2004, ApJ, 617, 746
Dickinson, M., Papovich, C., Ferguson, H. C., & Budavári, T. 2003, ApJ, 587, 25
Finger, G., Biereichel, P., Mehrgan, H., Meyer, M., Moorwood, A. F., Nicolini, G., & Stegmeier, J. 1998, Proc. SPIE, 3354, 87
Finger, G., Mehrgan, H., Meyer, M., Moorwood, A. F., Nicolini, G., & Stegmeier, J. 2000, Proc. SPIE, 4008, 1280
Franx, M., et al. 2003, ApJ, 587, L79
Hawarden, T. G., Leggett, S. K., Letawsky, M. B., Ballantyne, D. R., & Casali, M. M. 2001, MNRAS, 325, 563
Hodapp, K.-W., et al. 1996, New Astron., 1, 177
Ichikawa, T., et al. 2007, PASJ, 59, 1081
Ichikawa, T., Matsumono, D., Yanagisawa, K., Katsuno, Y., Suzuki, R., Tokoku, C., Asai, K., & Nishimura, T. 2003, Proc. SPIE, 4841, 376
Iye, M., et al. 2006, Nature, 443, 186
Kaifu, N., et al. 2000, PASJ, 52, 1
Kajisawa, M., et al. 2006, PASJ, 58, 951
Kashikawa, N., et al. 2006, ApJ, 648, 7
Kodama, T., Tanaka, I., Kajisawa, M., Kurk, J., Venemans, B., De Breuck, C., Vernet, J., & Lidman, C. 2007, MNRAS, 377, 1717
Kosugi, G., Sasaki, T., Aoki, T., Kawai, J. A., Koura, N., & Kusumoto, T. 1997, Proc. SPIE, 3112, 284
Kozlowski, L. J., et al. 1994, Proc. SPIE, 2268, 353
Kriek, M., et al. 2008, ApJ, 677, 219
Labbé, I., et al. 2003, AJ, 125, 1107
Madau, P., Ferguson, H. C., Dickinson, M. E., Giavalisco, M., Steidel, C. C., & Fruchter, A. 1996, MNRAS, 283, 1388
Malitson, I. H. 1965, J. Opt. Soc. Am., 55, 1205
Miyazaki, S., et al. 2002, PASJ, 54, 833
Motohara, K., et al. 2002, PASJ, 54, 315
Ouchi, M., et al. 2004, ApJ, 611, 660
Ren, D., & Allington-Smith, J. R. 1999, Opt. Eng., 38, 537
Steidel, C. C., Adelberger, K. L., Shapley, A. E., Pettini, M., Dickinson, M., & Giavalisco, M. 2003, ApJ, 592, 728
Steidel, C. C., Giavalisco, M., Dickinson, M., & Adelberger, K. L. 1996a, AJ, 112, 352
Steidel, C. C., Giavalisco, M., Pettini, M., Dickinson, M., & Adelberger, K. L. 1996b, ApJ, 462, L17
Suzuki, R., Tokoku, C., Ichikawa, T., & Nishimura, T. 2003, Proc. SPIE, 4841, 307
Tokoku, C., et al. 2006, Proc. SPIE, 6269, 62694N
Tokunaga, A. T., Simons, D. A., & Vacca, W. D. 2002, PASP, 114, 180
Tropf, W. J. 1995, Opt. Eng., 34, 1369
Uchimoto, Y. K., et al. 2008, PASJ, 60, 683
Willis, J. P., & Courbin, F. 2005, MNRAS, 357, 1348
Yamamuro, T., Sato, S., Zenno, T., Takeyama, N., Matsuhara, H., Maeda, I., & Matsueda, Y. 2006, Opt. Eng., 45, 3401
Yanagisawa, K., et al. 2006, Proc. SPIE, 6269, 62693Q
Yoshikawa, T., Omata, K., Konishi, M., Ichikawa, T., Suzuki, R., Tokoku, C., Uchimoto, Y. K., & Nishimura,T. 2006, Proc. SPIE, 6274, 62740Y